The history of the Tissint meteorite, from its crystallization on Mars to its exposure in space: New geochemical, isotopic, and cosmogenic nuclide data

Toni SCHULZ [1,2*], Pavel P. POVINEC [3], Ludovic FERRIÈRE [4], A. J. Timothy JULL [5,6],
Andrej KOVÁČIK [3,7], Ivan SÝKORA [3], Jonas TUSCH [2], Carsten MÜNKER [2], Dan TOPA [4], and
Christian KOEBERL [1,4]

[1]Department of Lithospheric Research, University Vienna, Althanstrasse 14, 1090 Vienna, Austria
[2]Institut für Geologie und Mineralogie, Universität zu Köln, Zülpicher Strasse 49b, 50674 Köln, Germany
[3]Faculty of Mathematics, Physics and Informatics, Department of Nuclear Physics and Biophysics, Comenius University,
SK-84248 Bratislava, Slovakia
[4]Natural History Museum, Burgring 7, 1010 Vienna, Austria
[5]Department of Geosciences, University of Arizona, Tucson, Arizona 85721, USA
[6]Hungarian Academy of Sciences, Institute for Nuclear Research, ICER, 4026 Debrecen, Hungary
[7]MicroStep-MIS, 84104 Bratislava, Slovakia
*Corresponding author. E-mail: toni.schulz@univie.ac.at

(*Received 11 April 2019; revision accepted 07 November 2019*)

Abstract–The Tissint meteorite fell on July 18, 2011 in Morocco and was quickly recovered, allowing the investigation of a new unaltered sample from Mars. We report new high-field strength and highly siderophile element (HSE) data, Sr-Nd-Hf-W-Os isotope analyses, and data for cosmogenic nuclides in order to examine the history of the Tissint meteorite, from its source composition and crystallization to its irradiation history. We present high-field strength element compositions that are typical for depleted Martian basalts (0.174 ppm Nb, 17.4 ppm Zr, 0.7352 ppm Hf, and 0.0444 ppm W), and, together with an extended literature data set for shergottites, help to reevaluate Mars' tectonic evolution in comparison to that of the early Earth. HSE contents (0.07 ppb Re, 0.92 ppb Os, 2.55 ppb Ir, and 7.87 ppb Pt) vary significantly in comparison to literature data, reflecting significant sample inhomogeneity. Isotope data for Os and W ($^{187}Os/^{188}Os = 0.1289 \pm 15$ and an $\varepsilon^{182}W = +1.41 \pm 0.46$) are both indistinguishable from literature data. An internal Lu-Hf isochron for Tissint defines a crystallization age of 665 ± 74 Ma. Considering only Sm-Nd and Lu-Hf chronometry, we obtain, using our and literature values, a best estimate for the age of Tissint of 582 ± 18 Ma (MSWD = 3.2). Cosmogenic radionuclides analyzed in the Tissint meteorite are typical for a recent fall. Tissint's pre-atmospheric radius was estimated to be 22 ± 2 cm, resulting in an estimated total mass of 130 ± 40 kg. Our cosmic-ray exposure age of 0.9 ± 0.2 Ma is consistent with earlier estimations and exposure ages for other shergottites in general.

INTRODUCTION

About 230 meteorites (including paired stones) are classified as Martian meteorites with only five of them being observed falls. Although large parts of the Martian surface are covered by sedimentary deposits, all known Martian meteorites so far are igneous rocks (more or less shocked and brecciated). Based on their chemical and mineralogical properties, Martian meteorites can be divided into distinct groups, from which more than three-quarters are basaltic shergottites (e.g., Chennaoui Aoudjehane et al. 2012; Irving et al. 2012). Based on their light rare earth element budget, they can be subdivided into depleted, intermediate, and enriched types. Shergottites also exhibit a significant range of, comparably young, crystallization ages from 165 ± 11 Ma for Shergotty (e.g., Nyquist et al. 2001; see also Brandon et al. [2012] for a recent data

compilation) to ages up to 574 ± 7 Ma for Dhofar 019 (Borg et al. 2001) and NWA 7635, with a reported Sm-Nd crystallization age of 2403 ± 140 Ma (Lapen et al. 2017). Signatures of ^{142}Nd indicate that Martian silicate differentiation occurred as early as ~4504 Ma (e.g., Borg and Drake 2005), possibly indicating that the comparably young shergottites preserved their mantle source compositions (acquired at ~4.5 Ga) throughout the history of Mars. Variable initial Sr, Nd, Hf, and Pb isotopic compositions, most likely point toward geochemically and isotopically distinct reservoirs that existed and are still preserved in the Martian mantle (e.g., Brennecka et al. 2014).

On July 18, 2011 at least 17 kg (e.g., Barrat et al. 2014) of material from Mars landed in Morocco, in the form of fragments of the Tissint meteorite. These fragments were rapidly recovered, allowing us to investigate a new and most likely unaltered sample from Mars, which was classified as a depleted picritic shergottite. It is an olivine-phyric shergottite with very magnesian olivine megacrysts in a matrix dominated by pyroxene and shocked plagioclase glass (maskelynite), with minor chromite, ilmenite, pyrrhotite, and phosphates (e.g., Chennaoui Aoudjehane et al. 2012; Balta et al. 2015; Liu et al. 2016). The meteorite shows strong evidence of shock metamorphism, including abundant (black) glassy melt pockets (up to cm in size), shock melt veins, and a large variety of high-pressure (HP) minerals and phases (e.g., Baziotis et al. [2013] and references therein).

Our study intends to cover different aspects of Tissint's history, including the incompatible high-field strength elements (HFSEs; Nb, Zr, Hf, Ta and W), which, together with an extended literature data set, allow us to challenge earlier inferences about a stagnant-lid regime on Mars in comparison to the early Earth. We also present new abundance data for a variety of highly siderophile elements (HSEs; Re, Os, Ir, and Pt), as well as Os and W isotopic compositions.

Constraints for the crystallization age of Tissint support an age of about 0.6 Ga (e.g., Grosshans et al. 2013; Park et al. 2013; Brennecka et al. 2014). In an attempt to reconcile the chronological relationship of Tissint, we present new Hf, Nd, and Sr isotope data for whole rock separates, as well as an internal Lu-Hf isochron.

A further focus of this study deals with the final stages of Tissint's history, encompassing ejection of Tissint from its parent body and exposure to cosmic rays. Cosmogenic radionuclides typically found in meteorites, such as ^{54}Mn ($T_{1/2}$ = 312.13 d), ^{22}Na ($T_{1/2}$ = 2.6029 yr), ^{60}Co ($T_{1/2}$ = 5.2711 yr), ^{14}C ($T_{1/2}$ = 5730 yr), ^{26}Al ($T_{1/2}$ = 0.717 Ma), and ^{10}Be ($T_{1/2}$ = 1.36 Ma), which are products of interactions of cosmic-ray particles (mostly protons and He-nuclei), are discussed in this study. They have been widely used to study the origin of meteorites, their orbital history, and cosmic-ray exposure ages. Their production rates depend on fluxes of galactic and solar cosmic-ray particles in the meteoroid, on the energy distribution of nuclear active particles, on the excitation functions, on the chemical composition, and on the position of the irradiated sample in the meteoroid body (e.g., Herzog 2003; Eugster et al. 2006; Leya and Masarik 2009; Leya et al. 2009; Welten et al. 2011). These radionuclides can be measured non-destructively by gamma-ray spectrometry (e.g., ^{22}Na, ^{26}Al, ^{60}Co, etc.), or with accelerator mass spectrometry (AMS) for longer lived radionuclides (e.g., Kutschera 2005; Jull and Burr 2013) that do not decay by gamma-ray emission (e.g., ^{14}C and ^{10}Be, but also ^{26}Al). In this study, we focused on cosmogenic radionuclides with half-lives from about 1 yr to about 0.7 Ma, which were still possible to analyze in 2013 (when the presented data were acquired) by non-destructive gamma-ray spectrometry (such as ^{54}Mn, ^{22}Na, ^{60}Co, and ^{26}Al) and by AMS (^{14}C). The aim was to determine the diameter and cosmic-ray exposure age of Tissint and to compare our results to similar studies that have been undertaken on Tissint and other shergottites (which cluster at 1.1 Ma, suggesting a single extraction event; e.g., Chennaoui Aoudjehane et al. 2012; Nishiizumi et al. 2012; Huber et al. 2013; Lapen et al. 2017).

SAMPLES AND ANALYTICAL METHODS

Samples

Two specimens of the Tissint meteorite from the Natural History Museum Vienna (NHMV, Austria) were used for this study; a 908.7 g stone (NHMV-N9388) and a 37.7 g fragment (NHMV-N9412). Both specimens are shown in Figs. 1a–d. Mineralogical and petrographic investigations were conducted on five polished thin sections, NHMV-N9402, N9404, N9405, N9406, and N9407 (i.e., the last four sections were prepared from the specimen NHMV-N9412, whereas the section NHMV-N9402 was prepared from another, smaller fragment of Tissint [NHMV_ID_#7994]) using optical microscopy (in both transmitted and reflected light), scanning electron microscope (SEM), and an electron microprobe.

The specimens NHMV-N9388 and NHMV-N9412 were also used for nondestructive gamma-ray spectrometry analyses. AMS was used for ^{14}C analysis of a small sample (188 mg) was taken from the NHM-Vienna_Tis10 fragment.

In addition, a fragment of 4.8 g was broken off from the specimen NHMV-N9412 (as far as possible from the fusion crust), from which ~2 g was gently crushed in an
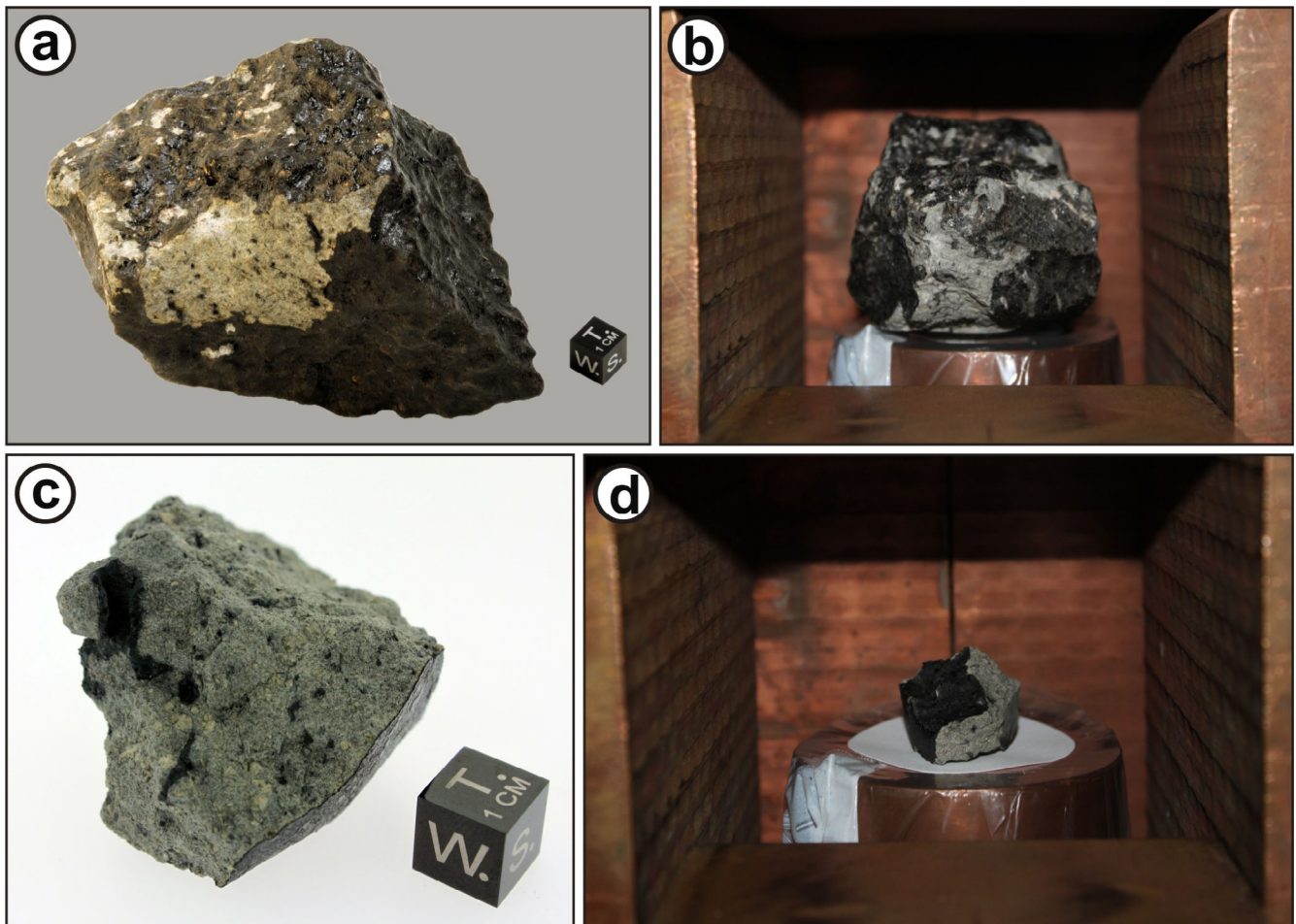
Fig. 1. Macrophotographs of the two specimens of the Tissint meteorite that were investigated in this study (both from the Natural History Museum Vienna). a) A 908.7 g oriented stone (NHMV-N9388) almost entirely covered with fresh fusion crust. b) The same specimen in the Bratislava gamma-spectrometry laboratory. c) A 37.7 g broken fragment (NHMV-N9412) showing the typical grayish matrix and a large, 1 cm in size, melt pocket (visible in the upper left of the photograph). d) The same fragment in the Bratislava gamma-spectrometry laboratory. (Color figure can be viewed at wileyonlinelibrary.com.)

agate mortar to obtain a homogeneous whole rock powder. A portion of this bulk powder was used for isotope dilution high field strength element (HFSE) and HSE analyses and Sr, Nd, Hf, and Os isotope composition measurements. In addition, nonmagnetic, moderately magnetic, and magnetic fractions were obtained using hand magnets with different magnetic intensities, and were used for the construction of a ^{176}Lu-^{176}Hf isochron.

Mineralogical and Petrological Investigations

Backscattered electron (BSE) images were obtained using a JEOL JSM 6610-LV SEM at the NHMV. A number of BSE images and X-ray maps of selected areas were obtained and element concentrations of minerals were analyzed quantitatively (in wavelength dispersive spectroscopy [WDS] mode) at the NHMV using a JEOL HyperProbe JXA 8530-F field-emission electron microprobe (FE-EPMA) after a careful BSE imaging examination for zoning and inclusions. An accelerating voltage of 15 kV, a beam current of 20 nA, a 1 μm beam diameter, and a counting time of 10 s for peak and 5 s for background were used for all element Kα lines. The following synthetic compounds Al_2O_3, Cr_2O_3, TiO_2, NiO, NaCl, KCl, and natural minerals tephroite Mn_2SiO_4, wollastonite $CaSiO_3$, Durango apatite $Ca_5(PO_4)_5F$, and Marjalahti olivine $(Mg,Fe)_2SiO_4$ were used as standards for Al, Cr, Ti, Ni, Na, K, Mn, Ca, Mg, Si, and Fe, respectively. The mean detection limits (in ppm) for measured elements (with SD in parentheses), calculated from 42 analyses points on olivine, pyroxene, maskelynite, chromite, and ilmenite, are: Si 63 (3), Ti 107 (15), Cr 174 (27), Al 48 (4), Fe 117 (14), Mn 105 (23), Ni 143 (14), Mg 48 (5), Ca 49 (5), Na 44 (3), and K 39 (4), respectively. Precision (relative) of analysis for major elements (Si, Al, Fe, Mg, and Ca) is typically better than 1%, but total

EPMA error is 1–2%. For trace elements (Ti, Cr, Mn, Ni, Na, and K), total EPMA error is larger (3–5%).

Geochemical and Isotopic Investigations

HFSE Analysis

Isotope dilution concentrations of an extended HFSE group (Nb, Zr, Hf, Ta, and W) were obtained from ~100 mg bulk powder. An additional Hf measurement and Lu were determined on another split of whole rock powder that was also used for the Sr-Nd-Hf isotope measurements. The full analytical procedure for HFSE and Lu concentration measurements was described in Münker et al. (2001) and Weyer et al. (2002). All samples were spiked using a mixed ^{183}W–^{180}Ta–^{180}Hf–^{176}Lu–^{94}Zr tracer. External precision and accuracy as determined by multiple digestions of different rock matrices (e.g., Weyer et al. 2002) are better than ±4% for Nb/Zr, ±0.6% for Zr/Hf, ±1% for Lu/Hf, and ±0.5% for Hf/W (2σ). Total blanks were generally <50 pg (Nb), <2 ng (Zr), <180 pg (Hf), <150 pg (Lu), and <100 pg (W).

HSE Analysis and ^{187}Os Isotope Measurements

About 0.5 g of the bulk powder was spiked with a mixed tracer composed of ^{185}Re, ^{190}Os, ^{191}Ir, and ^{194}Pt isotopes and digested in 7 ml inverse aqua regia (HNO_3-HCl: 5 + 2.5 ml) at 250 °C and 100–130 bars in an Anton-Paar high pressure asher for 12 h. After digestion, Os was separated from the other HSE using a CCl_4/HBr liquid extraction procedure (Cohen and Waters 1996). Osmium was further purified using a H_2SO_4/H_2CrO_4 microdistillation technique (Birck et al. 1997). After Os extraction, all other HSE were separated using a procedure adapted from the method of Pearson and Woodland (2000). Osmium was loaded as a bromide on Pt ribbon filaments covered with a $NaOH$/$Ba(OH)_2$ activator (Luguet et al. 2008). The ^{187}Os/^{188}Os isotope ratio and Os concentration measurements were carried out in negative mode using a Finnigan TRITON thermal ionization mass spectrometer (TIMS) at the Department of Lithospheric Research, University of Vienna (Austria). Isobaric interferences of ^{187}Re on ^{187}Os were monitored by measuring $^{185}ReO^{3-}$ (mass 233) and were corrected for. Mass fractionation was corrected offline using ^{192}Os/^{188}Os = 3.083 (Völkening et al. 1991; Luguet et al. 2008). The Os total procedural blank was ~0.8 pg.

Highly siderophile elements were measured using a Thermo Element XR SF-ICP-MS in single collector mode at the Steinmann-Institute at the University of Bonn (Germany), using methods described in Luguet et al. (2015). Total blanks for this study (n = 4) were ~4 pg for Re, ~3 pg for Ir, and ~22 pg for Pt. All reported concentration values are blank corrected.

^{182}W Isotope Measurements

Tungsten isotope measurements were performed using a Thermo Finnigan Neptune MC-ICPMS at the clean-lab facilities of the Institut für Geologie und Mineralogie at the University of Cologne (Germany). Tungsten was separated from about 250 mg of dissolved bulk powder, following the analytical protocol described in Tusch et al. (2019). Before measurement, samples were treated with a HNO_3–H_2O_2 mixture to remove organic compounds, then dried down and taken up for measurements in 0.5–1 ml 0.56 M HNO_3–0.24 M HF. Tungsten isotope compositions were typically measured with a signal intensity of ~1 V on ^{182}W. Small isobaric Os interferences on masses 184 and 186 were corrected for by monitoring the interference-free ^{188}Os. All reported ^{182}W/^{184}W ratios in Table 1 are reported as ε-unit deviations (i.e., 0.01%) relative to NIST 3163. Instrumental mass bias was corrected using the exponential law, normalizing to ^{186}W/^{184}W = 0.92767 (Völkening et al. 1991), and also to ^{186}W/^{183}W = 1.98594, to assess possible matrix effects or artifacts from incorrect mass bias corrections.

Lu-Hf, Nd, and Sr Isotope Analysis

Approximately 100 mg bulk powder as well as between ~50 and ~550 mg of the nonmagnetic, moderately magnetic, and magnetic fractions were spiked with a mixed ^{176}Lu-^{180}Hf tracer. In the case of the bulk powder sample, a ^{149}Sm-^{150}Nd tracer for isotope composition measurements of Hf and Nd, as well as isotope dilution generated concentrations for Lu, Hf, Sm, and Nd, was added. Complete digestion was achieved by table-top digestion following the procedure described in Münker et al. (2001) and Weyer et al. (2002). Lutetium and Hf were separated using Eichrom® Ln spec resin. In the case of the bulk powder sample, Sm and Nd were separated from the remaining matrix following the method of Pin and Zalduegui (1997). Lutetium, Hf, Sm, and Nd were measured using the Finnigan® Neptune multicollector ICP-MS in Bonn. For details on mass bias correction and typical external reproducibility, see Hoffmann et al. (2011) and Pittarello et al. (2013); for CHUR values and decay constants, see caption to Table 1. Total procedural blanks during the course of this study were ~8 pg for Lu, ~36 pg for Hf, and <50 pg for Sm and Nd. For ^{87}Sr/^{86}Sr isotope analysis, an ~100 mg aliquot of the bulk powder was digested in Savillex beakers using 5 ml of HF: HNO_3 (4:1) for 2 weeks at 110 °C on a hot plate. After acid evaporation, the residue was dissolved in 1 ml HNO_3 and after evaporation in 5 ml 6 N HCl. Strontium extraction was performed using BIORAD AG 50W-X8 (200–400 mesh) resin and 2.5 N and 4.0 N HCl as eluants. After loading on Re double filaments, the isotope ratio of ^{87}Sr/^{86}Sr was measured in static mode using a Finnigan

Table 1. Geochemical isotope data and isochron ages for Tissint from this study and in comparison to literature values.

	This study	Literature	Literature
HFSE			
Nb	0.174	0.28[A]	0.17[H]
Zr	17.4	23.14[A]	15[H]
Hf	0.7352	1.01[A]	0.67[H]
Ta	0.00879	0.0138[A]	0.010[H]
W	0.0444	–	0.061[H]
Nb/Zr	0.010	0.01[A]	0.01[H]
Zr/Hf	23.64	22.91[A]	22.4[H]
Hf/W	16.56	–	10.98[H]
HSE + ^{187}Os			
Re	0.068	0.23[B]	0.17[B]
Os	0.916	1.625[B]	1.093[B]
Ir	2.545	1.368[B]	0.374[B]
Pt	7.863	3.929[B]	1.294[B]
Os/Ir	0.360	1.188[B]	2.922[B]
Ir/Pt	0.324	0.348[B]	0.289[B]
^{187}Re/^{188}Os	0.356	0.926[B]	1.405[B]
^{187}Os/^{188}Os	0.1289 (15)	0.12954 (8)[B]	0.13008 (7)[B]
W isotopes			
ε^{183^1}W ± 2σ	0.17 ± 0.41		
ε^{183^2}W ± 2σ	0.11 ± 0.27		
ε^{182^3}W ± 2σ	1.41 ± 0.46	1.48 ± 0.10[C]	
ε^{182^4}W ± 2σ	1.36 ± 0.37		
^{87}Sr, ^{143}Nd, ^{176}Hf			
(^{87}Sr/^{86}Sr)$_i$	0.70092	0.700739[D] 0.700767[E]	0.700760[G]
ε(^{143}Nd)$_i$	+42.6	+41.6[F] +44.4[E]	+42.2[D]
ε(^{176}Hf)$_i$	+58.5	+58.0[F]	
Rb-Sr age (Ma)	–	560 ± 30[D] 495 ± 35[E]	621 ± 17[G] 559 ± 39[I]
Sm-Nd age (Ma)	–	616 ± 67[F] 472 ± 36[E]	587 ± 28[D]
Lu-Hf age (Ma)	665 ± 74	583 ± 86[F]	
Ar-Ar age (Ma)	–	610 ± 33[G]	

Concentrations of HFSE (high field strength elements) in ppm. HSE (highly siderophile elements) in ppb. 1 = ^{183}W/^{184}W rel. 6/4. 2 = ^{183}W/^{184}W rel. ^{186}W/^{183}W. 3 = ^{182}W/^{184}W rel. ^{186}W/^{184}W. 4 = ^{182}W/^{184}W rel 6/3. Sr-Nd-Hf initials were calculated using CHUR values of ^{147}Sm/^{144}Nd = 0.1960 and ^{176}Lu/^{177}Hf = 0.03360 and ^{143}Nd/^{144}Nd = 0.512630 and ^{176}Hf/^{177}Hf = 0.282785 (Bouvier et al. 2008) and decay constants of λ^{87}Rb = 0.01402 Ga^{-1}. 6.54 × 10^{-2}. λ^{147}Sm = 6.54 × 10^{-12} yr^{-1} and λ^{176}Lu = 1.867 ×10^{-11}yr^{-1} (Lugmair and Marti 1978; Begemann et al. 2001; Scherer et al. 2001). The initial ^{87}Sr/^{86}Sr was approximated using a measured ^{87}Sr/^{86}Sr ratio of 0.701035 for an unspiked whole rock sample and Rb and Sr concentrations as reported in Chennaoui Aoudjehane et al. (2012). A = Chennaoui Aoudjehane et al. (2012), B = Tait and Day (2018), C = Kruijer et al. (2017), D = Brennecka et al. (2014), E = Shih et al. (2014), F = Grosshans et al. (2013), G = Park et al. (2013), H = Yang et al. (2015), I = Suarez et al. (2019).

TRITON TIMS at the Department of Lithospheric Research, University of Vienna (Austria). A mean ^{87}Sr/^{86}Sr ratio of 0.710254 ± 0.000003 (n = 4) was determined for the NBS987 standard reference material. Within-run mass fractionation was corrected for using ^{88}Sr/^{86}Sr = 8.3752. The total procedural blank for Sr was <1 ng and, thus, considered negligible.

Cosmogenic Radionuclides

Gamma-Ray Spectrometry

Analyses of two specimens of the Tissint meteorite were carried out in the Low-Level Gamma-Ray Spectrometry Laboratory of the Department of Nuclear Physics and Biophysics of the Comenius University in Bratislava (Slovakia). A coaxial low-background high-purity germanium (HPGe) detector (PGT, USA) with relative detection efficiency of 70% (for 1332.5 keV gamma-rays of ^{60}Co) was used. The detector with anti-cosmic shielding operated in a large low-level background lead/copper shield with outer dimensions of 2 × 1.5 × 1.5 m (Povinec 2008; Povinec et al. 2009). A detailed description of the calibration procedures and applied corrections can be found in Kováčik et al. (2012, 2013). The quoted uncertainties include Monte Carlo efficiency calibration, coincidence summing corrections (for ^{22}Na, ^{26}Al, and ^{60}Co), self-absorption corrections, and counting statistics. The typical uncertainties were below 10%, and they varied depending on the sample size and the half-life of the investigated radionuclide. While for the small sample they were mainly due to counting statistics, for the large sample, the uncertainties associated with applied corrections were equal to uncertainties from counting statistics. The measuring time was 10 days for the bigger sample (NHMW-N9388) and 14 days for the smaller one (NHMW-N9412). The time used for decay corrections between the meteorite fall (July 18, 2011) and its analysis in the gamma-ray spectrometry laboratory was 1.94 yr.

Accelerator Mass Spectrometry

The cosmogenic ^{14}C was extracted in an RF induction furnace in a flow of oxygen, and passing the gases evolved over a CuO furnace to ensure conversion to CO_2. This gas was collected and measured volumetrically. The CO_2 was then converted to graphite and analyzed on a 3 MV AMS machine at the University of Arizona (USA). The full procedure for ^{14}C measurements is given in Jull et al. (1993, 2010).

RESULTS

Mineralogical and Petrological Data

Considering the large sample mass that was recovered of the Tissint meteorite, at least 17 kg (e.g., Barrat et al. 2014), some slight differences from one
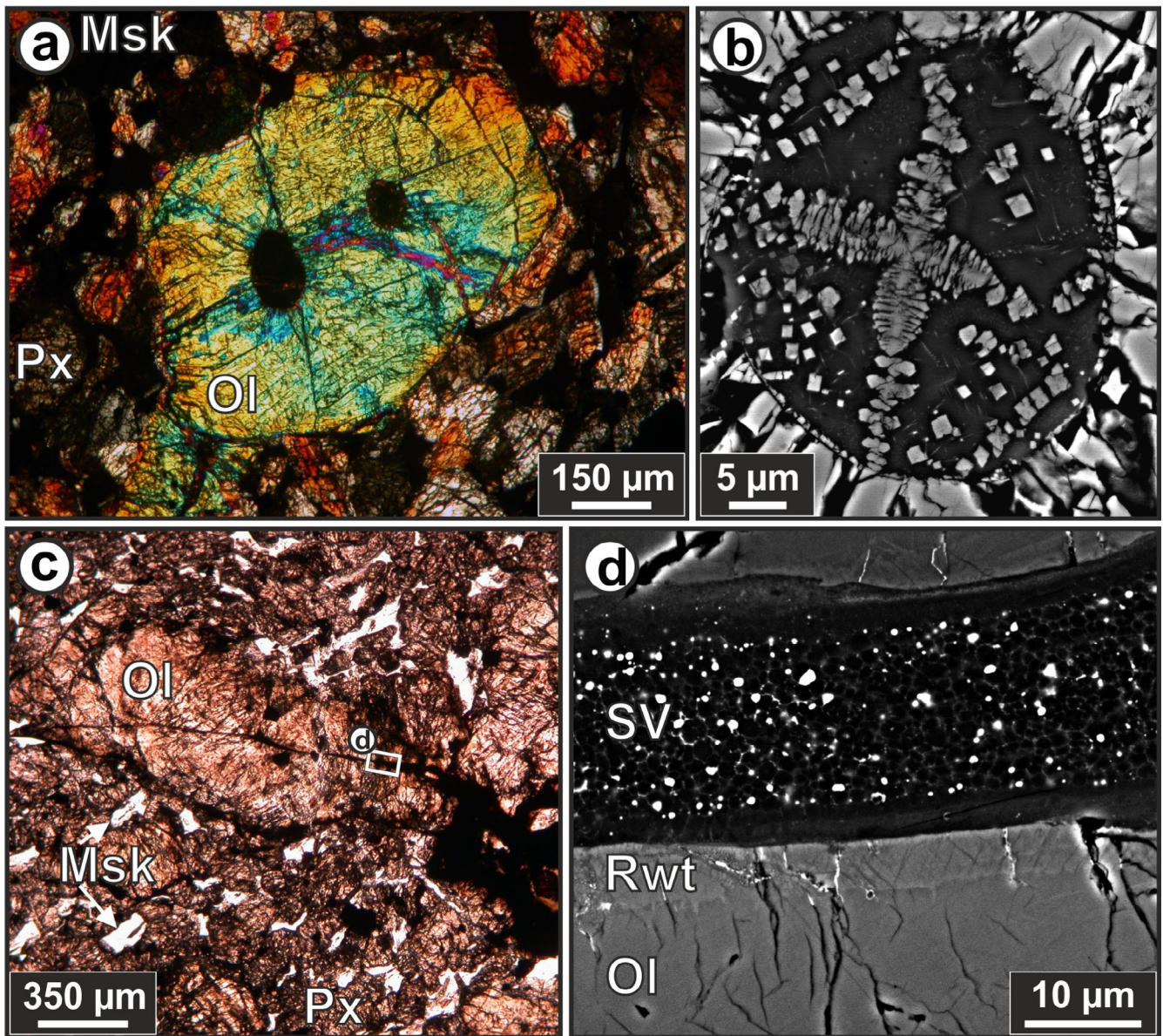
Fig. 2. Thin section photomicrographs with crossed polars (a), under plane-polarized light (c), as well as backscattered electron images (b and d) of some characteristic features of the sections of Tissint investigated in this study. a) Two large melt inclusions in an olivine (Ol) macrocryst surrounded by mainly pyroxene (Px), maskelynite (Msk), and olivine grains (thin section NHMV-N9407). b) Partially crystallized melt inclusion, with homogeneous glass and dendritic pyroxene, in an olivine macrocryst (thin section NHMV-N9405). c) Thin shock veins network cross-cutting the section, with a large impact-melt pocket in the lower right corner of the photograph (thin section NHMV-N9406). d) Enlarged part of (c) showing an olivine grain cross-cut by a shock vein (SV), with an ~5 μm margin of ringwoodite (i.e., light gray in the BSE image). (Color figure can be viewed at wileyonlinelibrary.com.)

fragment to another can be seen. In addition, in the present case, most of the investigated thin sections were prepared from a sample, that is, NHMV-N9412, that was used not only for the cosmogenic radionuclide measurements but also for the geochemical and isotopic investigations presented here.

All of the investigated thin sections show porphyritic textures (see Figs. 2a–d and 3a–f), as reported previously by, for example, Chennaoui Aoudjehane et al. (2012),

Balta et al. (2015), and Liu et al. (2016). Olivine megacrysts, up to 3 mm in size, are in most of the cases compositionally zoned (Figs. 3a–f) and as in most Martian meteorites, they contain melt inclusions, a few micrometers to more than 200 μm in size (Figs. 2a and 2b). Compositions of olivine in the investigated sections range from Fo_{79} to Fo_{43}, somewhat similar to Chennaoui Aoudjehane et al. (2012) and Liu et al. (2016). Our microprobe investigations of the melt inclusions show that
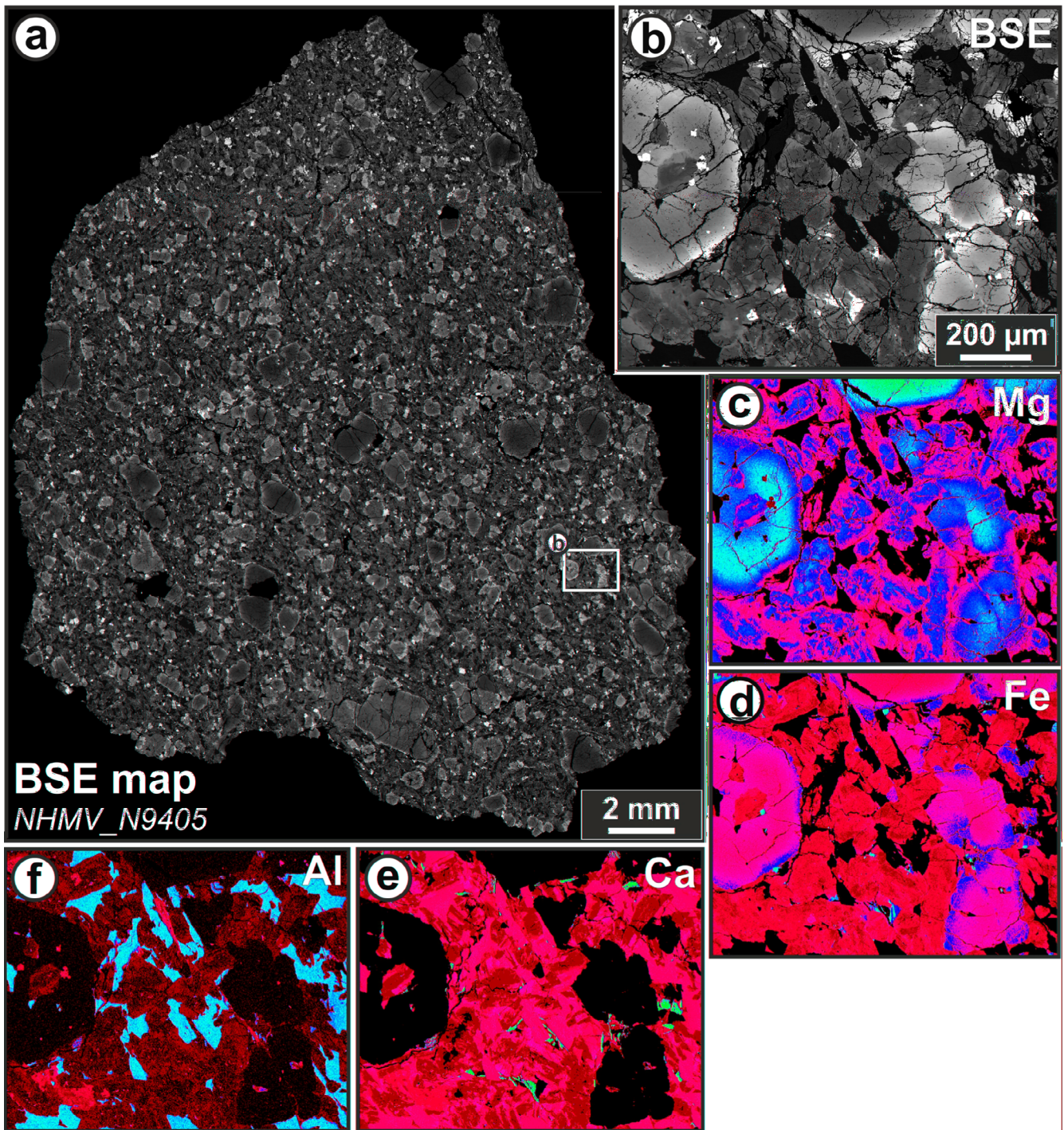
Fig. 3. Backscattered electron (BSE) images (a and b), wavelength dispersive spectroscopy (WDS), and energy dispersive X-ray spectroscopy (EDS) elemental distribution maps (c, d, and e, and f, respectively). a) BSE mosaic of thin section NHMV-N9405 showing the typical texture of Tissint with zoned olivine megacrysts. b) Enlarged part of (a) showing zoned olivine magacrysts (light gray), pyroxene (mid-gray), maskelynite (black), and some accessory minerals (white). c–e, and f) Elemental maps of Mg, Fe, Ca, and Al, respectively. Black to dark violet means no to relatively low amount, whereas yellow to red means relatively high amount. (Color figure can be viewed at wileyonlinelibrary.com.)

they are of different types, some being almost totally glassy (Si-rich), while others are partially crystallized, mainly consisting of pyroxene and plagioclase crystals (see Fig. 2b), as well as Ni-bearing Fe-sulfides and oxides (chromites). Similar observations were reported by Sonzogni and Treiman (2015). Pyroxenes occur as

euhedral to subhedral grains, up to about 1 mm in length. Compositions of pyroxenes in the matrix as well as pyroxenes within melt inclusions in olivine grains are shown in Table 2. All plagioclase grains have been converted by shock to isotropic glass (maskelynite). Compositions of maskelynite are also reported in Table 2. A number of thin shock veins, up to tens of μm in width, cross-cut the studied sections (Fig. 2). In some cases, HP minerals can be seen within or along the shock veins, such as ringwoodite (Fig. 2d). Shock melt pockets up to ~800 μm in size were detected in the investigated sections (see Fig. 2c), but they can be much larger, at least 1 cm in size as the one visible on specimen NHMV-N9412 (see Fig. 1c). A systematic study and discussion on shock features and high-pressure minerals and phases in Tissint can be found in Baziotis et al. (2013).

HFSE Data

High-precision Zr-Hf-Nb-Ta-W concentrations and selected interelement ratios are shown in Table 1 in comparison to literature values for Tissint, obtained using three different techniques (isotope dilution, ICP-MS, and LA-ICP-MS). A Zr/Hf ratio of 23.64, obtained in this study, compares to values of 22.4 from Yang et al. (2015) and ~22.9 from Chennaoui Aoudjehane et al. (2012). A Nb/Ta ratio of 19.7 from this study compares to a ratio of 15.9 from Chennaoui Aoudjehane et al. (2012) and a value of 17.0 for the Nb/Ta ratio obtained by Yang et al. (2015). The Hf/W ratio obtained in this study is 16.56. This value differs from the LA-ICP-MS derived ratio of 10.98 (Yang et al. 2015), probably arguing for varying amounts of contamination with impact melt veins in the analyzed samples splits, an inhomogeneous distribution of carrier phases and that, unlike Hf and Zr, Hf and W are harbored in different carrier phases.

HSE and Os and W Isotope Data

Concentrations for selected HSEs (HSE: Re, Os, Ir, and Pt), obtained on a whole rock powder from Tissint, are shown in Table 1. An Re concentration of 68 ppt was measured in conjunction with 0.916 ppb Os, 2.545 ppb Ir, and 7.863 ppb Pt. These values correspond to an Re/Os ratio of 0.074, an Os/Ir ratio of 0.360, and an Ir/Pt ratio of 0.324. The only literature HSE data available for Tissint bulk rock are reported in a recent study from Tait and Day (2018) and are also shown for comparison in Table 1. Applying isotope dilution and Carius Tubes digestion, these authors measured two aliquots of Tissint (of 0.3 and 1 g). They obtained contents of 230 and 170 ppt Re, 1.625 and 1.093 ppb

Os, 1.368 and 0.374 ppb Ir, and 3.929 and 1.294 ppb Pt, respectively. These values correspond to Re/Os ratios of 0.142 and 0.156, Os/Ir ratios of 1.188 and 2.922, and Ir/Pt ratios of 0.348 and 0.289. While the Ir/Pt ratio is comparably constant throughout all measurements, all other ratios (and corresponding concentrations) vary significantly, most likely due to nugget effects and/or sample inhomogeneity (i.e., in particular the variation of the amount of sulfides and HSE alloys, as well as in shock melt pockets and veins). Figure 4 shows a CI-normalized HSE pattern, comparing the various results mentioned above.

A $^{187}Os/^{188}Os$ ratio measured for Tissint in this study is 0.1289 (15) (see also Table 1). Within analytical uncertainty, this value is indistinguishable from values obtained by Tait and Day (2018) of 0.12954 (8) and 0.13008 (7), and is in line with the general trend for depleted shergottites, which typically range from ~0.128 to ~0.141 and corresponding $^{187}Re/^{188}Os$ ratios <2 (e.g., Tait and Day 2018).

Table 1 also shows the W isotope data obtained in this study. We obtained terrestrial $\varepsilon^{183}W$ signatures of +0.17 ± 0.41 (normalized to 186/184) and +0.11 ± 0.27 (normalized to $^{186}W/^{183}W$) and clearly resolved positive $\varepsilon^{182}W$ anomalies of +1.41 ± 0.46 (normalized to 186/184) and +1.36 ± 0.37 (normalized to $^{186}W/^{183}W$). The only reported W isotope data available for Tissint are from Kruijer et al. (2017). Our $\varepsilon^{182}W$ data nicely replicate the value of +1.48 ± 0.10 reported by these authors, confirming also the recently recognized large ^{182}W variability in Martian basalts with $\varepsilon^{182}W$ ratios ranging from 0.73 to 1.93 for depleted shergottites (Kruijer et al. 2017).

Lu-Hf, Nd, and Sr Isotope Data

Lutetium-Hf, Nd, and Sr isotopic results for a whole rock powder sample and three magnetically separated fractions from Tissint are shown in Tables 1 and 3.

Samarium and Nd concentrations for the whole rock powder sample, determined in this study using isotope dilution, are 0.717 and 1.114 ppm, respectively. This corresponds to an Sm/Nd ratio of 0.643 ($^{147}Sm/^{144}Nd$ = 0.389). These values are comparable to $^{147}Sm/^{144}Nd$ ratios of 0.378 and 0.380 determined by Grosshans et al. (2013) and 0.383 and 0.386 from Brennecka et al. (2014). An approximated initial $\varepsilon^{143}Nd$ value of +42.6 mirrors similar results of +41.6 from Grosshans et al. (2013) and +42.2 (Brennecka et al. 2014), and was calculated using Sm-Nd ages of 616 ± 67 Ma and 587 ± 28 Ma as determined by Grosshans et al. (2013) and Brennecka et al. (2014), respectively.

Table 2. Representative mineral compositions in the Tissint meteorite, in wt%, obtained by electron microprobe.

Mineral	Olivine						Pyroxene							Maskelynite			Chromite			Ilmenite
	Core			Rim			In matrix				In melt inclusions									
SiO2	39.8	39.9	39.7	34.8	36.8	35.4	54.8	51.9	57.4	53.1	54.8	52.4	54.3	55.4	55.5	57.3	0.21	0.19	0.24	0.12
Al2O3	0.06	0.03	0.02	0.05	0.02	bdl	0.82	0.97	0.35	1.31	0.91	3.42	1.21	27.7	27.3	26.6	9.07	8.68	7.74	0.15
MgO	40.4	40.6	41.3	21.0	26.7	21.0	23.1	15.0	30.2	20.3	23.9	17.4	22.2	0.38	0.39	0.28	7.11	4.11	6.42	2.86
FeO	19.3	19.4	18.6	43.6	36.2	43.5	16.7	20.2	10.2	16.2	16.0	12.2	15.4	1.25	1.28	0.92	24.7	28.7	25.2	42.4
MnO	0.41	0.40	0.38	0.83	0.67	0.75	0.57	0.57	0.27	0.53	0.58	0.48	0.55	0.02	0.03	0.04	0.25	0.33	0.24	0.74
CaO	0.21	0.21	0.20	0.53	0.24	0.37	4.08	10.7	1.59	7.46	3.76	13.4	6.09	11.3	11.4	10.7	0.01	0.05	0.02	0.10
Na2O	bdl	0.02	bdl	0.01	0.01	bdl	0.04	0.11	0.06	0.12	0.06	0.16	0.05	4.31	4.10	4.57	bdl	0.03	bdl	bdl
K2O	bdl	bdl	bdl	0.02	bdl	bdl	bdl	bdl	bdl	bdl	bdl	bdl	bdl	0.22	0.21	0.29	0.02	0.01	bdl	bdl
TiO2	0.04	0.03	0.02	0.13	0.07	0.06	0.15	0.67	bdl	0.24	0.16	0.58	0.25	0.20	bdl	0.02	0.98	1.25	0.70	55.0
Cr2O3	0.04	0.13	0.12	0.08	0.06	0.01	0.48	0.33	0.80	0.40	0.77	1.15	0.58	bdl	0.03	bdl	57.9	55.7	59.2	0.41
NiO	0.09	0.06	0.09	0.06	0.11	bdl	bdl	bdl	0.06	0.03	bdl	0.08	0.02	bdl	bdl	bdl	0.03	bdl	bdl	0.06
Total	100.4	100.9	100.5	101.1	100.9	101.1	100.7	100.4	100.9	99.6	100.9	101.2	100.6	100.8	100.5	100.8	100.3	99.0	99.7	101.8

Cations formula based on 24 oxygen atoms

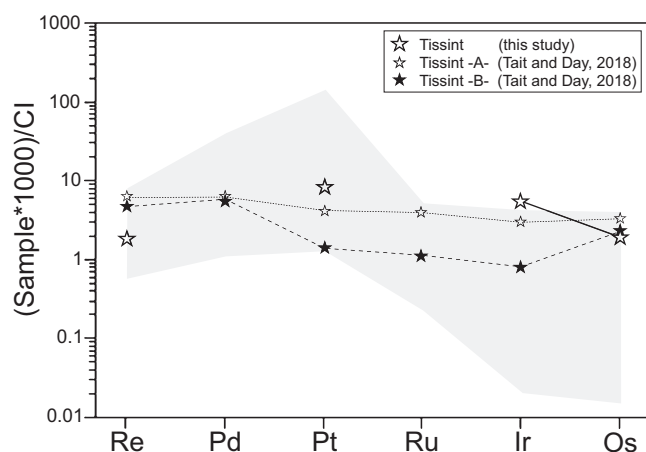| Mineral	Olivine						Pyroxene							Maskelynite			Chromite			Ilmenite
	Core			Rim			In matrix				In melt inclusions									
Si	6.087	6.084	6.058	6.008	6.102	6.086	7.966	7.878	8.008	7.878	7.931	7.659	7.909	7.463	7.497	7.671	0.044	0.040	0.049	0.023
Al	0.010	0.005	0.004	0.010	0.005		0.141	0.173	0.058	0.229	0.155	0.590	0.207	4.397	4.348	4.198	2.173	2.151	1.883	0.033
Mg	9.225	9.229	9.383	5.394	6.595	5.379	4.999	3.384	6.291	4.495	5.142	3.799	4.812	0.076	0.079	0.056	2.154	1.288	1.977	0.825
Fe	2.474	2.471	2.378	6.295	5.012	6.254	2.031	2.563	1.189	2.007	1.934	1.488	1.878	0.141	0.144	0.104	4.196	5.047	4.350	6.854
Mn	0.053	0.052	0.049	0.122	0.094	0.109	0.071	0.074	0.032	0.066	0.071	0.059	0.068	0.003	0.004	0.004	0.043	0.059	0.041	0.121
Ca	0.034	0.035	0.032	0.099	0.043	0.069	0.636	1.733	0.238	1.187	0.583	2.093	0.950	1.637	1.656	1.533	0.001	0.012	0.004	0.020
Na		0.006		0.003	0.004		0.010	0.033	0.017	0.035	0.017	0.045	0.013	1.126	1.073	1.187	0.004	0.011		
K				0.003										0.038	0.036	0.049	0.003	0.003		
Ti	0.004	0.003	0.002	0.016	0.009	0.008	0.016	0.077		0.027	0.017	0.064	0.027	0.021	0.022	0.021	0.149	0.198	0.109	7.990
Cr	0.005	0.016	0.014	0.011	0.007	0.002	0.055	0.040	0.088	0.047	0.089	0.133	0.067			0.002	9.304	9.258	9.658	0.063
Ni	0.011	0.007	0.011	0.008	0.015				0.007	0.003	0.003	0.009	0.003		0.004		0.004			0.009
Total	17.902	17.907	17.932	17.969	17.885	17.907	15.925	15.955	15.928	15.975	15.939	15.938	15.934	14.900	14.862	14.826	18.071	18.066	18.072	15.938

bdl = below detection limit.

Fig. 4. Chondrite-normalized highly siderophile element concentration patterns for Tissint whole rock. Data from this study and Tait and Day (2018). Gray shaded area represents the range for shergottites in general. Data from Tait and Day (2018) and references therein. Data for CI chondrite from Tagle and Berlin (2008).

Elemental concentrations of 0.153 ppm for Lu and 0.739 ppm for Hf, determined in this study using isotope dilution, compare to values of 0.155 and 0.187 ppm for Lu and 0.761 and 1.079 ppm for Hf determined by Grosshans et al. (2013) on whole rock separates from Tissint using the same technique. Chennaoui Aoudjehane et al. (2012) reported Lu and Hf concentrations measured by ICP-MS for two bulk samples of 0.160 and 0.190 ppm for Lu and 0.81 and 1.01 ppm for Hf. Corresponding Lu/Hf ratios for all studies, thus, are 0.207 (this study), 0.203 (Grosshans et al. 2013), 0.198 and 0.188 (Chennaoui Aoudjehane et al. 2012), and 0.173 (Grosshans et al. 2013). The varying concentrations and corresponding ratios might reflect apparent chemical heterogeneity within the Tissint meteorite. However, all ratios are slightly higher compared to the narrow range of Lu/Hf ratios among shergottites in general, which vary from ~0.103 to ~0.170 (Blichert-Toft et al. 1999). Using the bulk sample and three magnetically separated fractions (whose Lu/Hf ratios vary from 0.194 to 0.311), an Lu-Hf age of 665 ± 74 Ma was determined (Fig. 5). Although indistinguishable within error, this age is slightly higher compared to the 583 ± 86 Ma isochron determined by Grosshans et al. (2013), who used a three point linear regression and a lower $^{176}Lu/^{177}Hf$ spread between the separates. An age-corrected $\epsilon^{176}Hf$ value of +58.5 for Tissint, determined from data in this study, is in line with values reported by Grosshans et al. (2013), who reported a value of +58.0.

Finally, an initial $^{87}Sr/^{86}Sr$ ratio of 0.700746 was approximated, using a measured $^{87}Sr/^{86}Sr$ ratio of 0.701035 for an unspiked whole rock sample, and Rb as well as Sr concentrations as reported in Chennaoui Aoudjehane et al. (2012). These values are in good agreement with $^{87}Sr/^{86}Sr$

initial compositions from the literature of 0.700739 and 0.700760 (Park et al. 2013; Brennecka et al. 2014).

Cosmogenic Radionuclides

Results of analyses of cosmogenic radionuclides are presented in Table 4 (the measured activities were decay-corrected to July 18, 2011). Several gamma lines were identified in the gamma-ray spectrum of the Tissint meteorite. We specifically looked for cosmogenic ^{22}Na (the annihilation peak at 511 keV and the characteristic peak at 1274.5 keV), ^{26}Al (the annihilation peak at 511 keV and the characteristic peak at 1808.65 keV), and ^{54}Mn (peak at 835 keV). The ^{60}Co radionuclide (gamma energies at 1173.24 and 1332.50 keV) was not identified; therefore, only detection limits can be reported. The activities of ^{22}Na, ^{26}Al, and ^{54}Mn measured in the 37.7 and 908.7 g fragments are similar within the 1σ statistical uncertainty (Table 4). The average ^{22}Na and ^{26}Al activities are 65.4 ± 4.6 and 36.9 ± 3.1 dpm per kg, respectively. The $^{22}Na/^{26}Al$ activity ratio for the larger sample (measured with better precision) is 1.89 ± 0.05. This value is higher than the value expected for H chondrites (1.5), averaged by Bhandari et al. (2002) for several 11 yr solar cycles between 1970 and 2000. The observed high $^{22}Na/^{26}Al$ activity ratio observed in Tissint must be due to an undersaturation of ^{26}Al production, caused by its short cosmic-ray exposure age, as will be discussed later.

Unfortunately, short-lived radionuclides with half-lives shorter than 1 yr had already decayed when we conducted our measurements in 2013; thus, their activities were below detection limits. The ^{60}Co radionuclide (possible indicator of the burial depth of the specimen) was not identified, thus only detection limits are reported, at <0.2 and <1.9 dpm per kg (at 90% confidence level), for the large and the small specimens, respectively. The ^{14}C activity of 42.6 ± 0.4 dpm per kg measured in the large specimen is in agreement with the production rate of this radionuclide. The average activities of the primordial radionuclides in the Tissint meteorite are 280 ± 50 dpm per kg for ^{40}K, 2.4 ± 0.6 dpm per kg for ^{238}U, and 1.8 ± 0.6 dpm per kg for ^{232}Th. The obtained results for primordial radionuclides are comparable with the average concentrations reported by Wasson and Kallemeyn (1988) for chondrites. Chennaoui Aoudjehane et al. (2012) analyzed the same radionuclides in two small specimens of 29 and 58 g. Their results agree within quoted uncertainties with our data. They also observed high $^{22}Na/^{26}Al$ activity ratio (1.93 ± 0.11). Unfortunately, there are no more data available on short-lived radionuclides from other Martian meteorites.

Table 3. Lutetium-Hf isotopic compositions and Lu and Hf concentrations for separates from Tissint.

	Lu	Hf	Lu/Hf	$^{176}Lu/^{177}Hf$	$^{176}Hf/^{177}Hf$	εHf(t)
Bulk	0.1531	0.7389	0.2071	0.02941	0.284417 (4)	+58.4
Magnetic	0.1716	0.8844	0.1940	0.02754	0.284386 (10)	+58.1
Moderately magnetic	0.0352	0.1132	0.3110	0.04412	0.284605 (21)	+58.4
Nonmagnetic	0.0353	0.1453	0.2429	0.03413	0.284483 (16)	+58.6

Concentrations in ppm. See caption to Table 1 for calculation of initial ^{176}Hf values.
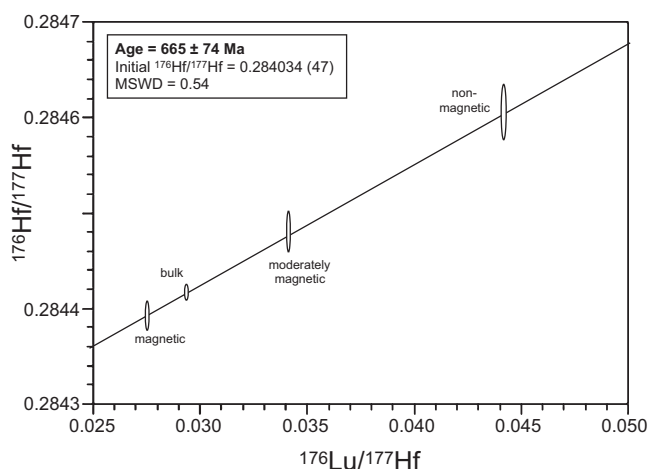
Fig. 5. Lu-Hf isochron for Tissint. The varyingly magnetic, and whole-rock samples define a ^{176}Lu-^{176}Hf age of 665 ± 74 Ma. The decay constant used for the ^{176}Lu isochron is 1.865×10^{-11} yr^{-1} (Scherer et al. 2001). The data were fitted using the Isoplot linear regression program (Ludwig 2008).

DISCUSSION

Age Constraints

Radiometric ages obtained using different chronometers and obtained from different studies (using different methods and samples) are all summarized in Table 1. Most Rb-Sr, Sm-Nd, Lu-Hf, and Ar-Ar ages overlap within analytical uncertainty. Weighted averages for these ages are 630 ± 56 Ma (MSWD = 2.1) for two Lu-Hf ages obtained from Grosshans et al. (2013) and this study, 577 ± 19 Ma (MSWD = 1.4) for two Sm-Nd ages from Brennecka et al. (2014) and Grosshans et al. (2013), and 606 ± 15 Ma (MSWD = 13) for three Rb-Sr ages obtained by Brennecka et al. (2014), Park et al. (2013), and Suarez et al. (2019). The high MSWD value for the Rb-Sr average may reflect Rb redistribution and external disturbances (e.g., Baziotis et al. 2013; Park et al. 2013), resulting in age determinations that vary outside their analytical uncertainties. Including a single Ar-Ar age of 610 ± 33 Ma from Park et al. (2013) also so far obtained age determinations average at

597 ± 47 Ma (MSWD = 6.6). Considering only Sm-Nd (excluding the age determination from Shih et al. 2014; see below) and Lu-Hf chronometry, we obtain a best estimate for the age of Tissint of 582 ± 18 Ma (MSWD = 3.2). Bouvier et al. (2005) reported Pb-Pb isotope alignments indicative of significantly older crystallization ages for shergottites of around 4.0 Ga. Bouvier et al. (2013) also reported a Pb-Pb age of ~4.33 Ga for Tissint. As Tissint fragments were recovered only 3 months after its fall, both studies excluded the possibility of significant contamination by terrestrial Pb, which would preclude meaningful age determinations. However, as discussed in Barrat et al. (2014), terrestrial contamination cannot be firmly ruled out. Bouvier et al. (2013) concluded that most mineral ages were reset by acidic aqueous solutions percolating through the Martian surface, yielding the more recent Rb-Sr, Sm-Nd, and Lu-Hf ages. Nevertheless, Bellucci et al. (2018) argued that all >4 Ga ages for Martian meteorites result from an incorrect interpretation of linear trends in the Pb isotopic diagrams. They concluded that these trends rather reflect mixing between radiogenic and unradiogenic reservoirs. Based on their interpretations, Bellucci et al. (2018) reported a corrected Pb model age for Tissint of 570 Ma, in line with all other age constraints reported in the literature for Tissint and including the age obtained in this study.

Shih et al. (2014) obtained Rb-Sr and Sm-Nd ages which are significantly lower (495 ± 35 Ma and 472 ± 36 Ma, respectively) compared to the values from this study and all other literature data. Although the reason for these age discrepancies is unknown, Suarez et al. (2019) speculated that a heterogeneous Tissint meteorite might explain the different ages. In this scenario, two different lava flows of differing ages could have hypothetically, been co-mingled during ejection (Suarez et al. 2019).

However, Tissint is not the oldest depleted shergottite. Dhofar 019, probably another depleted shergottite of similar age (Rb-Sr age of 525 ± 56 and Sm-Nd age of 586 ± 9 Ma; e.g., Borg et al. 2001) and NWA 7635, with a reported Sm-Nd crystallization age of 2403 ± 140 Ma (Lapen et al. 2017) extend the upper age range for depleted shergottites.

Table 4. Cosmogenic radionuclides in two Tissint specimens.

Sample	Mass (g)	^{22}Na	^{26}Al	^{54}Mn	^{60}Co	^{14}C
NHMV-N9412	37.7	62.3 ± 4.0	37.7 ± 2.8	52.4 ± 7.6	<1.9	
NHMV-N9388	908.7	68.5 ± 2.3	36.2 ± 1.3	55.7 ± 2.5	<0.2	42.6 ± 1.3

The measured activities were decay corrected to July 18, 2011. Uncertainties are given at the 1σ level.

Mantle Sources

Abundances of HFSE for Martian basalts were recently used to draw inferences about a stagnant-lid regime on Mars in comparison with the early Earth (Condie and Shearer [2017] and Condie [2018]). New HFSE abundance determinations for Tissint (from this study), and an extended literature data set, provide the basis for additional remarks on their hypotheses. Condie and Shearer (2017) and Condie (2018) compared Zr/Nb ratios of terrestrial oceanic non-arc basalts of varying ages and reported that two populations, corresponding to enriched or depleted mantle sources, can easily be traced back until about 2.5 Ga. Prior to this time, terrestrial mantle sources cannot be distinguished anymore in terms of their incompatible element ratios and both populations collapse into one single group. They argued that the divergence of the Zr/Nb ratios at ~2.5 Ga could possibly mark the onset of plate-tectonics, terminating a stagnant-lid regime on Earth that was characterized by relatively constant Zr/Nb ratios (of a primitive upper mantle-like signature scattering around ~20 as represented by data for ancient undifferentiated oceanic basalts). In support of their hypothesis, the authors claimed that the comparably narrow Zr/Nb spread of ancient terrestrial undifferentiated oceanic basalts is similar to the respective signatures of lunar mare basalts and Martian shergottites (which both were derived from solar system bodies with proposed stagnant-lid regimes).

Figure 6a is a diagram presenting an extended literature data set for Zr/Nb ratios for shergottites versus their ages. Depleted, intermediate, and enriched Martian shergottites can easily be differentiated. While depleted shergottites exhibit the oldest ages and largest spread in Zr/Nb ratios, enriched (and also intermediate) shergottites show comparably younger ages and a somewhat narrower Zr/Nb spread. However, the total Zr/Nb spread for shergottites range from ~15 to ~200 (e.g., ~135 for Y-980459 or ~184 for NWA 5990; Yang et al. 2015), instead of ~15 to ~70 as presented in Condie and Shearer (2017) and Condie (2018). The spread of the Zr/Nb ratios obtained in this study is also significantly higher than the Zr/Nb spread from ~5 to ~40 for ancient undifferentiated oceanic basalts from the Earth reported by the same authors. Thus, taking Zr/Nb signatures of ancient terrestrial non-arc basalts as an indicator for a stagnant-lid

regime during the Archean Earth might be, to some extent, problematic. Furthermore, Zr/Nb ratios in Martian shergottites need to be interpreted in the light of a postulated Nb enrichment on Mars compared to the Earth as advocated by Münker et al. (2003).

Figure 6b shows another diagram adopted from Condie and Shearer (2017) and expanded by a greater set of literature values for shergottites, plotting Zr/Nb ratios against Nb/Th ratios. Whereas Zr/Nb ratios are sensitive regarding the degree of partial melting, Nb/Th ratios are sensitive to fluid mobilization (due to enrichment of Th by fluids). As pointed out by Condie and Shearer (2017), rocks from stagnant-lid dominated solar system objects (such as Moon or Mars) plot near to the terrestrial primitive mantle composition, with Martian shergottite groups exhibiting a larger spread compared to lunar basalt, but only occasionally overlapping with the fields for terrestrial depleted and enriched mantle sources (also shown in the diagram after data from Condie and Shearer 2017). As Nb/Th ratios are particularly sensitive to fluid mobilization, Condie and Shearer (2017) also identified a third field, characteristic of the hydrated terrestrial mantle (also highlighted in Fig. 6b). Using the extended shergottite data set from the present study, it can be seen that the scatter of Martian shergottites (toward superchondritic Zr/Nb ratios and toward low Nb/Th ratios) is significantly higher than for the shergottite data presented by Condie and Shearer (2017). Niobium/Th ratios reported by Condie and Shearer (2017) range from ~8 to ~16. In fact, Tissint and a variety of other Martian shergottites (including relatively unaltered finds) plot at exceptionally high Zr/Nb ratios (>80) and Nb/Th ratios down to values of ~3 (e.g., for NWA 2800; Yang et al. 2015). Compared to the dataset presented earlier, some of these shergottites, including Tissint, overlap with the field characteristic for the terrestrial hydrated mantle. However, Martian shergottites derived from a hydrated mantle have so far not been recognized in the Martian meteorite collections (e.g., Condie and Shearer 2017) and it should be noted that crustal or other contamination during shergottite genesis could be responsible for the low Nb/Th ratios of some of the shergottites.

Irradiation Records

The radionuclides (^{14}C, ^{22}Na, ^{26}Al, and ^{54}Mn) identified in the Tissint fragments are produced by
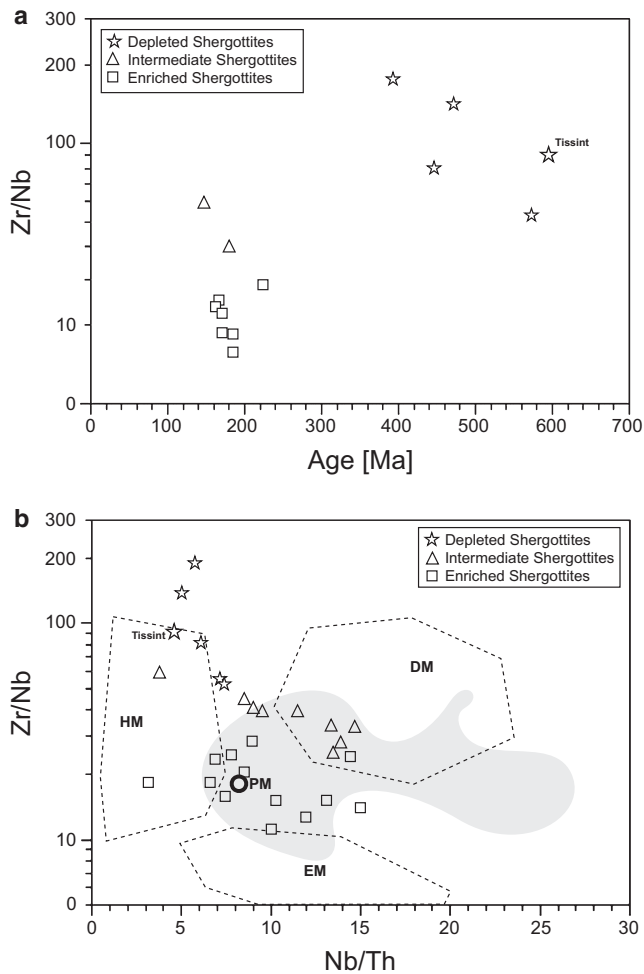
Fig. 6. a) Zr/Nb versus age diagram adopted after Condie (2018), showing data for Tissint and literature values for Martian basalts (shergottites). Zircon/Nb ratios are from this study (Tissint) and Yang et al. (2015). Ages for Martian meteorites are from Korochantseva et al. (2009) and from the compilation in Brandon et al. (2012). b) Zr/Nb versus Nb/Th diagram adopted after Condie (2018). EM = enriched terrestrial mantle, DM = depleted terrestrial mantle, and HM = hydrated terrestrial mantle. All values from Yang et al. (2015), Condie and Shearer (2017), and Condie (2018). PM: primitive mantle from McDonough and Sun (1995). Gray shaded area exemplifies the signature of ancient terrestrial undifferentiated oceanic basalts (3.4–2.5 Ga old; data from Condie and Shearer [2017] and Condie [2018]).

interaction of secondary cosmic-ray protons and neutrons mainly on O, S, Al, Si, and Fe nuclei. The production rates of ^{22}Na and ^{54}Mn, due to their short half-lives, also depend on variations of cosmic-ray fluxes during the 11 yr solar cycle. The production of ^{26}Al is due to its long half-life (0.717 Ma) is averaged during about 1.5 Ma. Although its production rate does not change significantly at larger depths, a steep rise with

depth is predicted by Monte Carlo simulations for subsurface layers (Leya and Masarik 2009).

We already mentioned that low ^{26}Al activity in the Tissint meteorite (36.2 ± 1.3 dpm per kg for the large fragment) indicates an undersaturated production due to its short cosmic-ray exposure (CRE) age. We estimated the CRE of the Tissint meteorite using the ^{26}Al method described by Herzog (2003). The CRE can be calculated from the equation $A = P(1-e^{-\lambda T})$, where A is the cosmogenic radionuclide activity, P is its production rate in the meteorite by cosmic-ray particles, λ is the decay constant, and T is the time of the meteorite irradiation equal to its CRE age. Figure 7 shows calculated ^{26}Al production rates for different radii of the Tissint meteorite following the Monte Carlo model of Leya and Masarik (2009), adjusting for its chemical composition of 21% of Si and 2.4% of Al (Avice et al. 2018). The measured ^{26}Al activity (36.2 ± 1.3 dpm per kg for the large fragment) shown in Fig. 7 is clearly outside of the range of calculated ^{26}Al production rates.

The pre-atmospheric radius of the Tissint meteorite was estimated using the following considerations. The ^{60}Co has been used as a depth indicator for fragments within the meteorite body, as well as for the estimation of its radius (e.g., Povinec et al. 2013, 2015a, 2015b). It has mainly been produced in the meteorite by the capture of thermal neutrons on ^{59}Co nuclei. This reaction peaks at larger depths in the meteorite and shows a strong dependence on its chemical composition. The ^{60}Co profile would, therefore, show ^{60}Co levels at the meteorite surface, and higher ^{60}Co levels close to the meteorite center, where the flux of thermal neutrons is at its maximum. The absence of ^{60}Co in the analyzed Tissint fragments would indicate either a small concentration of the target isotope (^{59}Co) in the meteorite and/or its small radius. The cobalt concentration in Tissint was measured to be 63.2 ppm (Avice et al. 2018), which is lower by about a factor of 10 when compared to H chondrites (Wasson and Kallemeyn 1988). The measured ^{60}Co limits (<0.2 dpm kg^{-1} for the large fragment and <1.9 dpm kg^{-1} for the small one, which is higher only due to small statistics), imply that in the case of Tissint, the ^{60}Co method is not useful for the determination of its radius. Fortunately, we have another cosmogenic radionuclide at hand, ^{14}C. Its activity of 42.6 ± 0.4 dpm kg^{-1} measured in the large fragment, following the approach described by Wieler et al. (1996), suggest for Tissint a radius of 20–24 cm. This value is in agreement with Nishiizumi et al. (2012) who estimated the pre-atmospheric radius using the ^{10}Be concentration measured in two fragments to be 15–25 cm. The mass of the Tissint meteoroid (expecting a ball shape with $r = 22$ cm and the average measured density of 3 g cm^{-3}) would be then 130 ± 40 kg.

Applying the estimated Tissint radius $r = 20$ and 24 cm in Fig. 7 for ^{26}Al depth profiles, we get for the ^{26}Al production rates values of 62–66 dpm kg^{-1}, respectively. The corresponding CRE age of the Tissint meteorite calculated with these production rates (following the above-described procedure) would be then 0.91 and 0.82 Ma, respectively. For the average production rate of 64 dpm kg^{-1}, the average CRE age is 0.9 ± 0.2 Ma, taking into account uncertainties of measurements and calculations of production rates.

Our estimation agrees with the CRE age of the Tissint meteorite calculated by Chennaoui Aoudjehane et al. (2012) using the method based on stable isotopes ^{3}He, ^{21}Ne, and ^{38}Ar (0.7 ± 0.3 Ma), which is in agreement with 1.10 ± 0.15 Ma based on the ^{10}Be method reported by Nishiizumi et al. (2012), and the average noble gas CRE age of 1.1 ± 0.1 Ma derived by Huber et al. (2013). These estimations are consistent with CRE ages of similar Martian meteorites (EETA79001, DaG 476-735, NWA 1195, 2046, 2626, 4925, 5789, SaU 005, and Yamato 980459; Becker and Repin 1984; Nishiizumi et al. 2011), which have an average CRE age of 1.05 ± 0.10 Ma (Nishiizumi et al. 2012). From these estimations, we may conclude that Tissint was likely ejected from Mars during the same impact event at around 1.05 ± 0.10 Ma as other depleted permafic olivine-phyric shergottites, although these small objects reached the Earth at different times. Lapen et al. (2017) pointed out that depleted shergottites that have ~1 Ma ejection ages have crystallization ages ranging from 350 Ma to 2.4 Ga ago, suggesting that there was a period of magmatic activity near the proposed ejection site (which would also have extracted Tissint) that spanned close to half of the history of Mars.

SUMMARY AND CONCLUSIONS

New mineralogical, HFSE, HSE, Sr-Nd-Hf-W-Os isotope, and cosmogenic radionuclide data for the Martian shergottite Tissint are reported in this study. Our results cover different aspects of Tissint's complex history, including its mantle source composition, age constraints, and its irradiation history. Furthermore, our results can be compared to literature data obtained for Tissint and other shergottites. We address issues regarding sample heterogeneity, interlaboratory comparisons, and the influence of different analytical techniques. Age constraints and geochemical data from this study also allow us to expand literature discussions covering different aspects of Martian evolution. The main observations reported in this paper can be summarized as follows:

1. HFSE data for Tissint, obtained in this study using isotope dilution, are compared to an extended
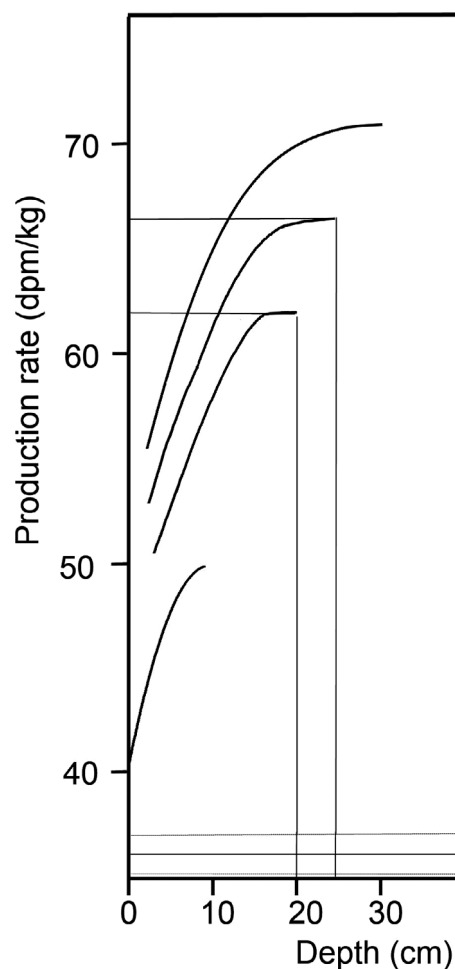

Fig. 7. Calculated production rates of cosmogenic ^{26}Al in Tissint meteorite (following the Leya and Masarik [2009] Monte Carlo model) for radii $r = 10$, 20, 25, and 30 cm. Measured ^{26}Al activity of 36.2 dpm per kg in the large fragment, as well as estimated ^{26}Al production rates (62 and 66 dpm per kg) for the meteorite radii of 20 and 25 cm, respectively, are also shown.

literature data set, revealing that Zr/Nb ratios for Martian basalts range from ~20 to ~200 (Tissint 100.0). The literature data set for shergottites (including Nb/Th ratios), presented in this study, reveals a significant Zr/Nb and Nb/Th spread, less diverse than, but comparable to, terrestrial oceanic basalts from the Archean, including those from hydrated mantle sources. This observation challenges earlier models postulating a stagnant-lid regime for the Archean Earth based on a comparison of Archean oceanic basalts with a limited shergottite data set exhibiting less diverse Zr/Nb and Nb/Th ratios.

2. Highly siderophile element (HSE) data (68 ppt Re, 0.916 ppb Os, 2.545 ppb Ir, and 7.863 ppb Pt) vary significantly in comparison to literature data for

Tissint, reflecting sample inhomogeneity, probably due to different amounts of shock melt glass pockets and HSE carrier phases in the bulk powders used for the different studies.

3. A $^{187}Os/^{188}Os$ ratio of 0.1289 ± 15 and an $\epsilon^{182}W$ value of $+1.41 \pm 0.46$ are both indistinguishable from literature data within analytical uncertainty. The $\epsilon^{182}W$ signature of Tissint confirms recent suggestions about widespread $^{182}W/^{184}W$ variations among Martian meteorites, requiring silicate differentiation on Mars within 20–40 million years after solar system formation (Kruijer et al. 2017).

4. An internal Lu-Hf isochron for Tissint defines a crystallization age of 665 ± 74 Ma. Considering only Sm-Nd and Lu-Hf chronometry, we obtain, using our and literature values, a best estimate for the age of Tissint of 582 ± 18 Ma (MSWD = 3.2). Initial values for $\epsilon^{176}Hf$, $\epsilon^{143}Nd$, and $^{87}Sr/^{86}Sr$ of +58.5, +42.6, and 0.700915, respectively, are in perfect agreement with literature data.

5. The pre-atmospheric size of the Tissint meteorite was estimated using cosmogenic ^{14}C to be 22 ± 2 cm, which would result in a total mass of 130 ± 40 kg.

6. The cosmic-ray exposure age estimated from the measured ^{26}Al levels in two fragments of the Tissint meteorite is 0.9 ± 0.2 Ma. This is consistent with age estimations for similar Martian meteorites (EETA79001, DaG 476-735, NWA 1195, 2046, 2626, 4925, 5789, SaU 005, and Yamato 980459; Becker and Repin 1984; Nishiizumi et al. 2011, 2012), suggesting that the group of depleted permafic olivine-phyric shergottites was ejected from Mars at the same time, around 1.05 ± 0.10 Ma.

Over the past few decades, our general knowledge of the mineralogy and geochemistry, as well as isotopic geochemistry of Martian rocks has been greatly increased by the study of meteorites but also thanks to the robotic missions on Mars. Our study shows that even well-studied meteorites such as Tissint still deserve to be investigated and reinvestigated.

Editorial Handling—Dr. Kevin Righter

REFERENCES

Avice G., Bekaert D. V., Chennaoui Aoudjehane H. B., and Marty B. 2018. Noble gases and nitrogen in Tissint reveal the composition of the Mars atmosphere. *Geochemical Perspectives Letters* 6:11–16.

Balta J. B., Sanborn M. E., Udry A., Wadhwa M., and McSween H. Y. Jr. 2015. Petrology and trace element geochemistry of Tissint, the newest shergottite fall. *Meteoritics & Planetary Science* 50:63–85.

Barrat J. A., Jambon A., Ferrière L., Bollinger C., Langlade J. A., Liorzou C., Boudouma O., and Fialin M. 2014. No Martian soil component in shergottite meteorites. *Geochimica et Cosmochimica Acta* 125:23–33.

Baziotis I. P., Liu Y., DeCarli P. S., Melosh H. J., McSween H. Y., Bodnar R. J., and Taylor L. A. 2013. The Tissint Martian meteorite as evidence for the largest impact excavation. *Nature Communications* 4:1404.

Becker R. H. and Pepin R. O. 1984. The case for a Martian origin of the shergottites: Nitrogen and noble gases in EETA 79001. *Earth and Planetary Science Letters* 69:225–242.

Begemann F., Ludwig K. R., Lugmair G. W., Min K., Nyquist L. E., Patchett P. J., Renne P. R., Shih C.-Y., Villa I. M., and Walker R. J. 2001. Call for an improved set of decay constants for geochronological use. *Geochimica et Cosmochimica Acta* 65:111–121.

Bellucci J. J., Nemchin A. A., Whitehouse M. J., Snape J. F., Bland P., Benedix G. K., and Roszjar J. 2018. Pb evolution in the Martian mantle. *Earth and Planetary Science Letters* 485:79–87.

Bhandari N., Murty S. V. S., Shukla P. N., Shukla A. D., Mahajan R. R., Sarin M. M., Srinivasan G., Suthar K. M., Sisodia M. S., Jha S., and Bischoff A. 2002. Itawa Bhopji (L3-5) chondrite regolith breccia: Fall, classification and cosmogenic records. *Meteoritics & Planetary Science* 37:549–564.

Birck J. L., Barman M. R., and Capmas F. 1997. Re-Os isotopic measurements at the femtomole level in natural samples. *Geostandards Newsletter* 21:19–27.

Blichert-Toft J., Gleason J. D., Telouk P., and Albarede F. 1999. The Lu-Hf isotope geochemistry of shergottites and the evolution of the Martian mantle-crust system. *Earth and Planetary Science Letters* 173:25–39.

Borg L. E. and Drake M. J. 2005. A review of meteorite evidence for the timing of magmatism and of surface or near-surface liquid water on Mars. *Journal of Geophysical Research* 110:E12S03.

Borg L. E., Nyquist L. E., Reese Y., Wiesmann H., Shih C.-Y., Ivanova M., Nazarov M. A., and Taylor L. A. 2001. The age of Dhofar 019 and its relationship to the other Martian meteorites (abstract #1144). 32nd Lunar and Planetary Science Conference. CD-ROM.

Bouvier A., Blichert-Toft J., Vervoort J. D., and Albarede F. 2005. The age of SNC meteorites and the antiquity of the Martian surface. *Earth and Planetary Science Letters* 240:221–233.

Bouvier A., Vervoort J. D., and Patchett P. J. 2008. The Lu-Hf and Sm-Nd isotopic composition of CHUR: Constraints from unequilibrated chondrites and implications for the bulk composition of terrestrial planets. *Earth and Planetary Science Letters* 273:48–57.

Bouvier A., Blichert-Toft J., Albarede F., El Goresy A., Agee C. B., and Gillet P. 2013. U-Th-Pb evolution requires very old age for newly found depleted shergottites (abstract #2421). 44th Lunar and Planetary Science. CD-ROM.

Brandon A., Puchtel I., Walker R., Day J., Irving A., and Taylor L. 2012. Evolution of the Martian mantle inferred from the ^{187}Re–^{187}Os isotope and highly siderophile element abundance systematics of shergottite meteorites. *Geochimica et Cosmochimica Acta* 76:206–235.

Brennecka G. A., Borg L. E., and Wadhwa M. 2014. Insights into the Martian mantle: The age and isotopics of the meteorite fall Tissint. *Meteoritics & Planetary Science* 49:412–418.

Chennaoui Aoudjehane H., Avice G., Barrat J. A., Boudouma O., Chen G., Duke M. J. M., Franchi I. A., Gattacceca J., Grady M. M., Greenwood R. C., Herd C. D. K., Hewins R., Jambon A., Marty B., Rochette P., Smith C. L., Sautter V., Verchovsky A., Weber P., and Zanda B. 2012. Tissint Martian meteorite: A fresh look at the interior, surface, and atmosphere of Mars. *Science* 338:785–788.

Cohen A. and Waters F. 1996. Separation of osmium from geological materials by solvent extraction for analysis by thermal ionisation mass spectrometry. *Analytica Chimica Acta* 332:269–275.

Condie K. C. 2018. A planet in transition: The onset of plate tectonics on Earth between 3 and 2 Ga? *Geoscience Frontiers* 9:51–60.

Condie K. C. and Shearer C. K. 2017. Tracking the evolution of mantle sources with incompatible element ratios in stagnant-lid and plate-tectonic planets. *Geochimica et Cosmochimica Acta* 213:47–62.

Eugster O., Herzog G. F., Marti K., and Caffee M. W. 2006. Irradiation records, cosmic ray exposure ages, and transfer time of meteorites. In *Meteorites and the early solar system II*, edited by Lauretta D. and McSween H. Y. Jr. Tucson, Arizona: University of Arizona Press. pp. 829–851.

Grosshans T. E., Lapen T. J., Andreasen R., and Irving A. J. 2013. Lu-Hf and Sm-Nd ages and source compositions for depleted shergottite Tissint (abstract #2872). 44th Lunar and Planetary Science Conference. CD-ROM.

Herzog G. F. 2003. Cosmic-ray exposure ages of meteorites. In Davis A. M. (Ed.), *Meteorites, comets, and planets*, edited by Holland H. D. and Turekian K.K. *Treatise on Geochemistry*, vol. 1. Heidelberg: Springer. pp. 347–380.

Hoffmann J. E., Münker C., Polat A., Rosing M., and Schulz T. 2011. The origin of decoupled Hf-Nd isotope compositions in Eoarchean rocks from southern West Greenland. *Geochimica et Cosmochimica Acta* 75:6610–6628.

Huber L., Irving A. J., Maden C., and Wieler R. 2013. Noble gas cosmic ray exposure ages for five shergottites and evidence for trapped Martian atmosphere in Tissint (abstract #1534). 44nd Lunar and Planetary Science Conference. CD-ROM.

Irving A. J., Kuehner S. M., Tanaka R., Herd C. D. K., Chen G., and Lapen T. J. 2012. The Tissint depleted permafic olivine-phyric shergottite: Petrologic, elemental and isotopic characterization of a recent Martian fall in Morocco (abstract #2510). 43rd Lunar and Planetary Science Conference. CD-ROM.

Jull A. J. T., and Burr G. S. 2013. Mass spectrometry instruments VI. In *Accelerator mass spectrometry*, edited by Turekian K. K. and Holland H. Treatise of Geochemistry, vol. 15. Amsterdam: Elsevier. pp. 375–383.

Jull A. J. T., Donahue D. J., Cielaszyk E., and Wlotzka F. 1993. ^{14}C terrestrial ages and weathering of 27 meteorites from the southern high plains and adjacent areas (USA). *Meteoritics* 28:188–195.

Jull A. J. T., McHargue L. R., Bland P. A., Greenwood R. C., Bevan A. W. R., Kim K. J., Giscard M. D., LaMotta S. E., and Johnson J. A. 2010. Terrestrial ^{14}C and ^{14}C-^{10}Be ages of meteorites from the Nullarbor, Australia. *Meteoritics & Planetary Science* 45:1271–1283.

Korochantseva E. V., Trieloff M., Buikin A. I., and Hopp J. 2009. Shergottites Dhofar 019, SaU 005, Shergotty, and Zagami: ^{40}Ar-^{39}Ar chronology and trapped Martian atmospheric and interior argon. *Meteoritics & Planetary Science* 44:293–321.

Kováčik A., Sýkora I., Povinec P. P., and Porubčan V. 2012. Non-destructive gamma-spectrometry analysis of cosmogenic radionuclides in fragments of the Košice meteorite. *Journal of Radioanalytical and Nuclear Chemistry* 293:339–345.

Kováčik A., Sýkora I., and Povinec P. P. 2013. Monte Carlo and experimental efficiency calibration of gamma-spectrometers for non-destructive analysis of large volume samples of irregular shapes. *Journal of Radioanalytical and Nuclear Chemistry* 298:665–672.

Kruijer T. S., Kleine T., Borg L. E., Brennecka G. A., Irving A. J., Bischoff A., and Agee C. B. 2017. The early differentiation of Mars inferred from Hf-W chronometry. *Earth and Planetary Science Letters* 474:345–354.

Kutschera W. 2005. Progress in isotope analysis at ultra-trace level by AMS. *International Journal of Mass Spectrometry* 242:145–160.

Lapen T. J., Righter M., Andreasen R., Irving A. J., Satkoski A. M., Beard B. L., Nishiizumi K., Jull T. A. J., and Caffee M. W. 2017. Two billion years of magmatism recorded from a single Mars meteorite ejection site. *Science Advances* 3:2, e1600922.

Leya I. and Masarik J. 2009. Cosmogenic nuclides in stony meteorites revisited. *Meteoritics & Planetary Science* 44:1061–1086.

Leya I., Welten K. C., Nishiizumi K., and Caffee M. W. 2009. Cosmogenic nuclides in the solar gas-rich H3-6 chondrite breccia Frontier Mountain 90174. *Meteoritics & Planetary Science* 44:77–85.

Liu Y., Baziotis I. P., Asimow P. D., Bodnar R. J., and Taylor L. A. 2016. Mineral chemistry of the Tissint meteorite: Indications of two-stage crystallization in a

closed system. *Meteoritics & Planetary Science* 51:2293–2315.

Ludwig K. R. 2008. Isoplot/Ex Ver. 3.70. Berkely Geochronology Center. Special Publication no. 4.

Lugmair G. W. and Marti K. 1978. Lunar initial ^{143}Nd/^{144}Nd: Differential evolution of the lunar crust and mantle. *Earth and Planetary Science Letters* 39:349–357.

Luguet A., Nowell G. M., and Pearson D. G. 2008. ^{184}Os/^{188}Os and ^{186}Os/^{188}Os measurements by negative thermal ionisation mass spectrometry (N-TIMS): Effects of interfering element and mass fractionation corrections on data accuracy and precision. *Chemical Geology* 248:342–362.

Luguet A., Behrens M., Pearson D. G., König S., and Herwartz D. 2015. Significance of the whole rock Re–Os ages in cryptically and modally metasomatised cratonic peridotites: Constraints from HSE–Se–Te systematics. *Geochimica et Cosmochimica Acta* 164:441–463.

McDonough W. F. and Sun S.-S. 1995. The composition of the Earth. *Chemical Geology* 120:223–253.

Münker C., Weyer S., Scherer E., and Mezger K. 2001. Separation of high field strength elements (Nb, Ta, Zr, Hf) and Lu from rock samples for MC-ICPMS measurements. *Geochemistry Geophysics Geosystems* 2. https://doi.org/10.1029/2001GC000183.

Münker C., Pfänder J. A., Weyer S., Büchl A., Kleine T., and Mezger K. 2003. Evolution of planetary cores and the Earth-Moon system from Nb/Ta systematics. *Science* 301:84–87.

Nishiizumi K., Nagao K., Caffee M. W., Jull A. J. T., and Irving A. J. 2011. Cosmic-ray exposure chronologies of depleted olivine-phyric shergottites (abstract #2371). 42nd Lunar and Planetary Science Conference. CD-ROM.

Nishiizumi K., Caffee M. W., and Irving A. J. 2012. Exposure history of Tissint: Evidence for 1.1 million year launch pairing with other depleted olivine-phyric shergottites (abstract). *Meteoritics & Planetary Science* 47:5349.

Nyquist L. E., Bogard D. D., Shih C. Y., Greshake A., Stoffler D., and Eugster O. 2001. Ages and geologic histories of Martian meteorites. *Space Science Reviews* 96:105–164.

Park J., Herzog G. F., Nyquist L. E., Shih C.-Y., Turrin B., Lindsay F. N., Delaney J. S., Swisher C. C., and Agee C. 2013. Ar-Ar and Rb-Sr ages of the Tissint olivine-phyric Martian shergottite (abstract). *Meteoritics & Planetary Science* 48:5320.

Pearson D. G. and Woodland S. J. 2000. Solvent extraction/anion exchange separation and determination of PGEs (Os, Ir, Pt, Pd, Ru) and Re-Os isotopes in geological samples by isotope dilution ICP-MS. *Chemical Geology* 165:87–107.

Pin C. and Zalduegui J. F. S. 1997. Sequential separation of light rare-earth elements, thorium and uranium by miniaturized extraction chromatography: Application to isotopic analyses of silicate rocks. *Analytica Chimica Acta* 339:79–89.

Pittarello L., Schulz T., Koeberl C., Hoffmann J. E., and Münker C. 2013. Petrography, geochemistry, and Hf-Nd isotope evolution of drill core samples and target rocks from the El'gygytgyn impact crater, NE Chukotka, Arctic Russia. *Meteoritics & Planetary Science* 48:1160–1198.

Povinec P. P. 2008. Low-level gamma-ray spectrometry for environmental samples. *Journal of Radioanalytical and Nuclear Chemistry* 276:771–777.

Povinec P. P., Sýkora I., Porubčan V., and Ješkovský M. 2009. Analysis of ^{26}Al in meteorite samples by coincidence gamma-ray spectrometry. *Journal of Radioanalytical and Nuclear Chemistry* 282:805–808.

Povinec P. P., Laubenstein M., Ferrière L., Brandstätter F., Sýkora I., Kováčik A., Jull A. J. T., Topa D., and Koeberl C. 2013. The Chelyabinsk meteoroid – What do we learn from the recovered meteorite fragments? (abstract) *Meteoritics & Planetary Science Supplements* 76:5196.

Povinec P. P., Masarik J., Sýkora I., Kovacik A., Beňo J., Laubenstein M., and Porubčan V. 2015a. Cosmogenic radionuclides in the Košice meteorite: Experimental investigations and Monte Carlo simulations. *Meteoritics & Planetary Science* 50:880–892.

Povinec P. P., Laubenstein M., Jull A. J. T., Ferrière L., Brandstätter F., Sýkora I., Masarik J., Beňo J., Kováčik A., Topa D., and Koeberl C. 2015b. Cosmogenic radionuclides and mineralogical properties of the Chelyabinsk (LL5) meteorite: What do we learn about the meteoroid? *Meteoritics & Planetary Science* 50:273–286.

Scherer E., Münker C., and Mezger K. 2001. Calibration of the Lutetium-Hafnium clock. *Science* 293:683–687.

Shih C.-Y., Nyquist L. E., Park J., and Agee C. B. 2014. Sm-Nd and Rb-Sr isotopic systematics of a heavily shocked Martian meteorite Tissint and petrogenesis of depleted shergottites (abstract #1184). 45th Lunar and Planetary Science Conference. CD-ROM.

Sonzogni Y. and Treiman A. 2015. Small melt inclusions can record bulk magma compositions: A planetary example from the Martian basalt (shergottite) Tissint. *Meteoritics & Planetary Science* 50:1880–1895.

Suarez S. E., Lapen T. J., Righter M., Beard B. L., and Irving A. J. 2019. Assessing the heterogeneity of the Tissint shergottite strewnfield using Rb-Sr, Sm-Nd and Lu-Hf isotope systematics (abstract #3028). 50th Lunar and Planetary Science Conference. CD-ROM.

Tagle R. and Berlin J. 2008. A database of chondrite analyses including platinum group elements, Ni Co, Au, and Cr: Implications for the identification of chondritic projectiles. *Meteoritics & Planetary Science* 43:541–559.

Tait K. T. and Day J. M. D. 2018. Chondritic late accretion to Mars and the nature of shergottite reservoirs. *Earth and Planetary Science Letters* 494:99–108.

Tusch J., Sprung P., van de Löcht J., Hoffmann J. E., Boyd A. J., Rosing M. T., and Münker C. 2019. Uniform ^{182}W isotope compositions in Eoarchean rocks from the Isua region, SW Greenland: The role of early silicate differentiation and missing late veneer. *Geochimica et Cosmochimica Acta* 257:284–310.

Völkening J., Walczyk T., and Heumann K. G. 1991. Osmium isotope ratio determinations by negative thermal ionization mass spectrometry. *International Journal of Mass Spectrometry and Ion Processes* 105:147–159.

Wasson J. T. and Kallemeyn G. W. 1988. Compositions of chondrites. *Philosophical Transactions of the Royal Society of London* 325:535–544.

Welten K. C., Caffee M. W., Hillegonds D. J., McCoy T. J., Masarik J., and Nishiizumi K. 2011. Cosmogenic radionuclides in L5 and LL5 chondrites from Queen Alexandra Range, Antarctica: Identification of a large L/LL5 chondrite shower with a preatmospheric mass of approximately 50,000 kg. *Meteoritics & Planetary Science* 46:177–196.

Weyer S., Münker C., Rehkämper M., and Mezger K. 2002. Determination of ultra low Nb, Ta, Zr, and Hf concentrations and the chondritic Zr/Hf and Nb/Ta ratios by isotope dilution analyses with multiple collector ICP-MS. *Chemical Geology* 187:295–313.

Wieler R., Graf T., Signer P., Vogt S., Herzog G. F., Tuniz C., Fink D., Fifield L. K., Klein J., Middleton R., Jull A.

J. T., Pellas P., Masarik J., and Dreibus G. 1996. Exposure history of the Torino meteorite. *Meteoritics & Planetary Science* 31:265–272.

Yang S., Humayun M., Righter K., Jefferson G., Fields D., and Irving A. J. 2015. Siderophile and chalcophile element abundances in shergottites: Implications for Martian core formation. *Meteoritics & Planetary Science* 50:691–714.